

Supplemental Online Material for:

Fluorescent biological aerosol particle concentrations and size distributions measured with an ultraviolet aerodynamic particle sizer (UV-APS) in central Europe

J. A. Huffman^{1*}, B. Treutlein^{1,2}, and U. Pöschl¹

¹*Max Planck Institute for Chemistry, Biogeochemistry Department, Becherweg 27, D-55128 Mainz, Germany*

²*Now at Ludwig Maximilians University, Institute for Physical Chemistry, Munich, Germany*

*Corresponding author: a.huffman@mpic.de, +49 (6131) 305 376

[Huffman et al., Atmos. Chem. Phys., 10, 3215-3233, 2010.](#)

Published Version: April 6, 2010

S1. Additional Experimental Details

In the course of long term operation, a “Check Flow” signal on the instrument occasionally indicated that the actual flow rates exceeded the specified range. In such instances, the inner flow was found to have increased up to ~1.25 Lpm, while the total flow remained in the range 4.9 – 5.0 Lpm. The desired flow rates were re-established by cleaning the APS nozzle with compressed air. Sampling took place at the Max Planck Institute for Chemistry in building N, room 408.

S2. Data Processing and Analysis, Additional Details

S2.1 Data File Format and Processing

The TSI AIM software was used to record original data and to export the correlated data of particle number concentration ($dN/d\log D_a$) and fluorescence versus aerodynamic diameter for each 5 minute measurement from the original data file (TSI *.A12 format) into an ASCII text file (*.txt format with comma delimiter). Further processing, statistical analysis, and plotting of the data were performed with Igor software (Wavemetrics Inc., Version 6.0.5). A user-written Igor program was used to sum $dN/d\log D_a$ into two-dimensional matrices of particle size vs. measurement date and time for further analysis. Lognormal fits were performed with the standard fitting algorithm of Igor [fit parameters: $x_0 = D_g$, width = $2.303 \cdot \sqrt{2} \log \sigma_g$, $A = 2.303 \cdot N / (\sqrt{\pi} \cdot \text{width})$].

S2.2 Size Bin Information

Based on the time-of-flight measurement, particles detected by the UV-APS are binned in 52 size channels within the instrument electronics, which are logarithmically scaled with the lower cut-off and geometric mean diameters listed in Supplemental Table S1. The geometric width of the size channels, $d\log D_a$, was 0.25 for the lowermost channel ($< 0.54 \mu\text{m}$) and 0.03125 for all other 51 channels (up to $19.81 \mu\text{m}$). For each detected particle, the fluorescence intensity measured after the aerodynamic sizing was recorded on a relative scale of 64 channels, ranging from non-detectable (channel 1) to maximum (channel 64) fluorescence signal. The fluorescence intensity detector was used as adjusted and delivered by the manufacturer and tested upon instrument setup with fluorescent polystyrene latex particles ($0.5 \mu\text{m}$, TSI p/n 2609053). A typical multi-point size calibration curve for particles $< 3.5 \mu\text{m}$ is shown in Figure S1. Absolute fluorescence intensity data are not recorded by the UV-APS, and the instrument is not calibrated for quantitative number concentration detection. Measured fluorescence sensitivity is affected by several instrument parameters, of which the UV pulse detector (UVP) voltage is automatically optimized (Agranovski et al., 2003). Over the course of the measurement period the UVP voltage was 181 ± 38 .

S2.3 Detection Limits

For the interpretation and scaling of size distribution data and plots (Section 3.2) we have calculated the lowest detectable concentrations (LDC) measurable in each size channel of the UV-APS during the five-minute sample measurements performed in this study assuming the ability to detect a single particle. For the incremental particle number concentration per size channel (dN) as well as for the integrated particle number concentration (N), the LDC is given by the inverse of the sample volume

passing through the measurement cell: $LDC_N = LDC_{dN} = 2 \times 10^{-4} \text{ cm}^{-3}$. With regard to size distributions, the lowest detectable value is given by division of LDC_{dN} through the geometric width of the size channel: $LDC_{dN/d\log D_a} = 8 \times 10^{-4} \text{ cm}^{-3}$ for channel 1 ($< 0.54 \mu\text{m}$, $d\log D_a = 0.25$) and $LDC_{dN/d\log D_a} = 6.4 \times 10^{-3} \text{ cm}^{-3}$ for size channels 2-52 ($0.54 - 19.81 \mu\text{m}$, $d\log D_a = 0.03125$), used for further analysis.

The LDC of particle mass scales with the third power of the aerodynamic diameter of detected particles. For each size channel LDC_{dM} has been calculated by multiplication of LDC_{dN} with the volume of the aerodynamic equivalent sphere with geometric midpoint diameter ($D_{a,g}$) and density of 1 g cm^{-3} . The values of LDC_{dM} are listed in Table S1, ranging from 3 pg m^{-3} (channel 1) to $0.8 \mu\text{g m}^{-3}$ (channel 52). The corresponding values of $LDC_{dM/d\log D_a}$ range from 11 pg m^{-3} to $26 \mu\text{g m}^{-3}$. The lowest detectable integrated mass concentration, LDC_M , is effectively given by the lowest value of LDC_{dM} in the range of size channels which have been used for data analysis in this study (channels 2-52): 17 pg m^{-3} . The LDC values are the same for FBAPs and total aerosol particles (TAPs, including non-fluorescent aerosol particles) and are listed here for individual measurements at the conditions of this study. The LDC of data points averaged over a longer time period will scale inversely with the number of measurements recorded (n). Note that all particle sizes given here are $D_{a,g}$, but will be simplified as D_a . UV-APS fluorescence detection limits are also discussed in detail by Ho et al. (2002).

S3. Additional Results and Discussion, Additional Details

S3.1 Overview of Number Concentrations

Through-out the measurement period the total coarse particle number concentration, $N_{T,c}$, varied mostly within a relatively narrow range of values between $0.37 - 1.30 \text{ cm}^{-3}$ (25 – 75th percentiles). The month of November exhibited maxima up to 14 cm^{-3} during November 27 – December 2. Several events of high $N_{T,c}$ maxima ($> 4 \text{ cm}^{-3}$) and high sustained $N_{T,c}$ background ($> 2 \text{ cm}^{-3}$) also occurred between October 11 – November 13, with the largest occurring the early mornings of October 30 and November 1. The lowest values of $N_{T,c}$ were detected November 13 – 14, with minima as low as 0.03 cm^{-3} .

In contrast to total particles, the FBAP number concentration, $N_{F,c}$, exhibited more consistent behavior (Figs. S7a and 2b; $0.012 - 0.033$, 25 – 75th percentiles). The highest $N_{F,c}$ concentrations were observed October 25 – 27, 30 – 31, and November 8, with minima at least $> 0.3 \text{ cm}^{-3}$ each day. The lowest sustained (> 6 hours) values of $N_{F,c}$ were detected on November 2 and 13 when the concentration dropped to 0.0015 cm^{-3} and remained below $\sim 0.005 \text{ cm}^{-3}$ for 8 and 16 hours, respectively. This period coincides with a several day period of high $N_{T,c}$. $N_{F,c}/N_{T,c}$ varied typically in the range of 1.7 – 5.5% (25 – 75th percentiles). The highest consistent FBAP fractions were observed August 12 – 19, where maxima exceeded 12% each day and 23% at several points. Other consistently high ($> 5\%$) $N_{F,c}/N_{T,c}$ periods were observed October 20 – 27 and November 14 – 19.

Figure 3 shows plots similar to Figure 1, but showing campaign median values for each hour of the day. A daily $N_{F,c}$ peak of 0.029 cm^{-3} at 7:00 LT is clearly evident above a relatively flat background of $0.017 - 0.018 \text{ cm}^{-3}$ (Fig. S10a). $N_{F,c}/N_{T,c}$ shows a similar trend, with a peak at 7:00 of 4.4% above an early morning background of 2.6%. A second, minor peak of 3.9% in the FBAP coarse particle number ratio is evident at 17:00. This is a result of the corresponding decrease in $N_{T,c}$ at this

time, while the $N_{F,c}$ is relatively constant. Figure S10b shows that the 7:00 peak in $N_{F,c}$ is a result of a peak in $dN_F/d\log D_a$ at $3.2 \mu\text{m}$. The peak at this size is the most prominent particle size through all hours of the day, but increases at night and is highest in the mid-morning (5:00 – 10:00). In each plot of monthly median values the $\sim 3 \mu\text{m}$ peak is dominant at all times of the day, but retains a diel cycle with a peak in the mid-morning. Of the four months of $N_{F,c}$ measurements, August exhibits the highest diel peak at 0.040 cm^{-3} during 7:00 – 8:00, as well as the largest relative diel swing ($\times 3.5$ between diel minimum and maximum). September, however, showed relatively little diel swing in $N_{F,c}$ ($\times 1.6$) and the lowest diel peak of any month (0.019 cm^{-3}). The November pattern was unique, however, because the $\sim 3 \mu\text{m}$ peak shows two distinct diel maxima at 7:00 and 15:00. $N_{F,c}$ shows two peaks with relatively equal height (0.025 and 0.028 cm^{-3} , respectively) caused by the increased concentration of $\sim 3 \mu\text{m}$ particles. $N_{F,c}$ then drops off steeply after 15:00 and rises steeply again immediately before 7:00. The November pattern also shows a more prominent peak at $\sim 0.8 \mu\text{m}$ during night time hours that is not as clearly seen in the other months.

The maxima of $dN_T/d\log D_a$ during August and September occurred at 4:00, while the peak shifted increasingly earlier in October and November to 2:00 and 21:00, respectively (a second peak in September is also observed at 9:00).

S3.2 Overview of Mass Concentrations

The highest peaks in $M_{T,c}$ came during a period from October 25 – 27 when daily morning maxima exceeded $100 \mu\text{g m}^{-3}$ each day and reached $270 \mu\text{g m}^{-3}$ on October 26. The periods from August 28 – September 1 and September 6 – 7 also exhibited high daily $M_{T,c}$ peaks of $> 45 \mu\text{g m}^{-3}$. October 2 – 3 and November 13 – 14 exhibited the lowest $M_{T,c}$ values at $< 1 \mu\text{g m}^{-3}$ for $\sim 12, 24$ hours, respectively and daily minima regularly dropped to $< 1.5 \mu\text{g m}^{-3}$ over the course of the measurement period.

Monthly mean $M_{T,c}$ values varied by a factor of ~ 1.5 from a minimum of $5.3 \mu\text{g m}^{-3}$ in August to $8.2 \mu\text{g m}^{-3}$ in November. The 95th percentile values were 2.1 – 2.3 times higher than the mean values of $M_{T,c}$ in each case. The mean value of $M_{F,c}$ ($1.9 \mu\text{g m}^{-3}$) in October represents the only month above the range of $0.92 - 1.1 \mu\text{g m}^{-3}$.

$M_{F,c}$ for August (Fig. S16a) shows the clearest morning peak compared to the other three months, but also shows relatively little diel cycle in $M_{F,c}/M_{T,c}$ (18.0% minimum, 22.0% maximum). The contribution of mass by the larger particles ($7 - 9 \mu\text{m}$) is most significant in September and November, and least significant in August.

S4. SOM References

Agranovski, V., Ristovski, Z., Hargreaves, M., Blackall, P. J. and Morawska, L.: Real-time measurement of bacterial aerosols with the UVAPS: performance evaluation, *Journal of Aerosol Science*, 34, 301-317, 10.1016/s0021-8502(02)00181-7, 2003.

Ho, J.: Future of biological aerosol detection, *Anal. Chim. Acta*, 457, 125-148, 2002.

Supplemental Online Material Table and Figure Captions

Table S1: UV-APS instrument statistics shown for each of 52 particle size channels. $D_{a,g}$ shows geometric median value of the upper and lower range for aerodynamic particle diameter. $D_{a,low}$ refers to the lower particle size bound. Lowest detectable concentration (LDC) as absolute value (dM) and normalized to width of size bin ($dM/d\log D_a$). Campaign mean values of $dN_{T,c}$, $dN_{F,c}$, $dM_{T,c}$, $dM_{F,c}$ shown per size bin.

Figure S1: Example of standard particle size calibration curve for UV-APS. Aerodynamic diameter (D_a) measured by UV-APS plotted vs. D_a of polystyrene latex spheres (PSL) of varying diameter. Data points show nebulized PSLs, and black trace is a linear fit to the data. Physical diameter (D_p) of PSLs were converted to D_a using a density, $\rho = 1.05 \text{ g/cm}^3$ and dynamic shape factor, $X = 1.0$. Linear fit of data has equation: $y = 1.028x + 0.0043$.

Figure S2: Time series of FBAP number concentrations for the entire measurement period using fluorescence bins ≥ 2 (to compare with “standard” analysis using bins ≥ 3). **(a)** Integrated $N_{F2,c}$ on left axis (green) and FBAP fraction of TAP number ($N_{F2,c} / N_{T,c}$) on right axis (black). **(b)** Image plot of FBAP number with aerodynamic diameter shown logarithmically on y-axis and date on x-axis. Color scale shows $dN_{F2}/d\log D_a$. Details are analogous to Figure 12.

Figure S3: Time series of FBAP number concentration factor increase using fluorescence bins ≥ 2 compared with using fluorescence bins ≥ 3 . **(a)** Ratio of integrated $N_{F2,c} / N_{F,c}$. **(b)** Image plot of ratio between $dN_{F2,c}$ and $dN_{F,c}$ with aerodynamic diameter shown logarithmically on y-axis and date on x-axis. Color scale shows factor increase in $N_{F2,c}$, with white values shown at an arbitrary point for visual clarity.

Figure S4: Size distribution of factor increase in of integrated $dN_{F2,c}$ compared to $dN_{F,c}$. Campaign-mean size distribution for $dN_{F2,c}/d\log D_a$ for fluorescence bins ≥ 2 divided by $dN_{F,c}/d\log D_a$ for fluorescence bins ≥ 3 .

Figure S5: Scatter plots of N_F vs. N_T for particle diameters below **(a)** and above **(b)** $1.0 \mu\text{m}$, respectively. $D_a \leq 0.965 \mu\text{m}$ and $D_a \geq 1.037 \mu\text{m}$ geometric mid-point of UV-APS size channels 9 and 10, respectively. $N_{F,<0.965}$ particle number exhibiting fluorescence in the fine particle mode ($< 1.0 \mu\text{m}$) and $N_{T,<0.965}$ all particles in size mode. $N_{F,>1.037}$ and $N_{T,>1.037}$, coarse mode ($> 1.0 \mu\text{m}$). Data points are colored by date of measurement; note that later points obscure earlier points. Black lines are linear fits to all data in each plot, with equations and Pearson’s R-squared values as follows: (a) $y = 0.000918x + 0.000786$, $R^2 = 0.51$, (b) $y = 0.0102x + 0.0178$, $R^2 = 0.17$.

Figures S6: Scatter plots of N_F vs. N_T for particle diameters below **(a)** and above **(b)** $0.75 \mu\text{m}$, respectively. Details are analogous to Figure S5, except that $D_a \leq 0.723 \mu\text{m}$ and $D_a \geq 0.777 \mu\text{m}$ geometric mid-point of UV-APS size channels 5 and 6, respectively. (a) $y = 0.000867x + 0.000150$, $R^2 = 0.87$, (b) $y = 0.00221x + 0.0224$, $R^2 = 0.11$.

Figure S7: Time series of FBAP number concentrations and size distributions for the entire measurement period (3 August – 4 December 2006). **(a)** Integrated coarse FBAP concentration (1-20 μm , $N_{F,c}$) on left axis (green) and FBAP fraction of TAP number ($N_{F,c} / N_{T,c}$) on right axis (black). Note that axes are logarithmically scaled and off-set from one another. Each data point represents a five-minute measurement. **(b)** FBAP size distribution with date on x-axis, aerodynamic diameter on y-axis, and color scale of $dN_F/d\log D_a$ with white values set to $LDC_{dN/d\log D_a} = 6.4 \times 10^{-3} \text{ cm}^{-3}$. Dashed black line at $1.0 \mu\text{m}$ shows particle size cut-off below which fluorescent particles were not considered FBAP due to interference with non-biological aerosol.

Figure S8: Time series of TAP number concentrations and size distributions for the entire measurement period (3 August – 4 December 2006). **(a)** Integrated coarse TAP concentration (1-20 μm , $N_{T,c}$) on left axis (green) and FBAP fraction of TAP number ($N_{F,c} / N_{T,c}$) on right axis (black). Note that axes are logarithmically scaled and off-set from one another. Each data point represents a five-minute measurement. **(b)** TAP size distribution with date on x-axis, aerodynamic diameter on y-axis, and color scale of $dN_T/d\log D_a$ with white values set to $LDC_{dN/d\log D_a} = 6.4 \times 10^{-3} \text{ cm}^{-3}$. Dashed black

line at 1.0 μm shows particle size cut-off below which fluorescent particles were not considered FBAP due to interference with non-biological aerosol.

Figure S9: Time series of TAP number concentrations (panel top halves) and size distributions (panel bottom halves) for each month of the measurement period (plots analogous to Fig. S7): **(a)** August, **(b)** September, **(c)** October, and **(d)** November (extending to December 4).

Figure S10: Diel cycles of FBAP number concentrations and size distributions for the entire measurement period (hourly median values vs. local time of day). **(a)** Integrated coarse FBAP concentration (1-20 μm , $N_{F,c}$) on left axis (green) and FBAP fraction of TAP number ($N_{F,c} / N_{T,c}$) on right axis (black). **(b)** FBAP size distribution with hour of day on x-axis, aerodynamic diameter on y-axis and color scale of $dN_F/d\log D_a$ with white values set to 0.001 cm^{-3} for visual clarity. Dashed black line at 1.0 μm shows particle size cut-off below which fluorescent particles were not considered FBAP due to interference with non-biological aerosol. Light-green shaded area shows FBAP concentration variability as the area between 25th – 75th percentile traces.

Figure S11: Diel cycles of TAP number concentrations and size distributions for the entire measurement period (hourly median values vs. local time of day). **(a)** Integrated coarse TAP concentration (1-20 μm , $N_{T,c}$) on left axis (green) and FBAP fraction of TAP number ($N_{F,c} / N_{T,c}$) on right axis (black). **(b)** TAP size distribution with hour of day on x-axis, aerodynamic diameter on y-axis and color scale of $dN_T/d\log D_a$ with white values set to 0.5 cm^{-3} for visual clarity. Dashed black line at 1.0 μm shows particle size cut-off below which fluorescent particles were not considered FBAP due to interference with non-biological aerosol. Light-blue shaded area shows FBAP concentration variability as the area between 25th – 75th percentile traces.

Figure S12: Diel cycles of TAP number concentrations (panel top halves) and size distributions (panel bottom halves) for each month of the measurement period (plots analogous to Fig. S9): **(a)** August, **(b)** September, **(c)** October, and **(d)** November. Light-blue shaded area shows FBAP concentration variability as the area between 25th – 75th percentile traces.

Figure S13: Diel cycles of FBAP mass concentrations (panel top halves) and size distributions (panel bottom halves) for each month of the measurement period (plots analogous to Fig. S9): **(a)** August, **(b)** September, **(c)** October, and **(d)** November.

Figure S14: Time series of TAP mass concentrations and size distributions for the entire measurement period (3 August – 4 December 2006). **(a)** Integrated coarse TAP concentration (1-20 μm , $M_{T,c}$) on left axis (green) and FBAP fraction of TAP mass ($M_{F,c} / M_{T,c}$) on right axis (black). Note that axes are logarithmically scaled and off-set from one another. Each data point represents a five-minute measurement. **(b)** TAP size distribution with date on x-axis, aerodynamic diameter on y-axis, and color scale of $dN_T/d\log D_a$ with white values set to 6.4×10^{-3} $\mu\text{g m}^{-3}$ for visual clarity. Dashed black line at 1.0 μm shows particle size cut-off below which fluorescent particles were not considered FBAP due to interference with non-biological aerosol.

Figure S15: Time series of TAP number concentrations (panel top halves) and size distributions (panel bottom halves) for each month of the measurement period (plots analogous to Fig. S12): **(a)** August, **(b)** September, **(c)** October, and **(d)** November (extending to December 4).

Figure S16: Diel cycles of FBAP mass concentrations (panel top halves) and size distributions (panel bottom halves) for each month of the measurement period (plots analogous to Fig. 8): **(a)** August, **(b)** September, **(c)** October, and **(d)** November. Light-green shaded area shows FBAP concentration variability as the area between 25th – 75th percentile traces.

Figure S17: Normalized FBAP number concentration, $dN_F/d\log D_a$ for exemplary period #1 (Fig. 9a – b).

Figure S18: Characteristic FBAP number size distribution patterns observed during exemplary periods #7 and #8. Left panels show time series of $N_{F,c}$, $N_{F,c} / N_{T,c}$ ratio and $dN_F/d\log D_a$ on days of interest (analogous to Fig. 1), and black vertical lines indicate time periods over which exemplary size distributions were averaged ($dN_F/d\log D_a$ vs D_a , right panels). Red traces represent mean values, green traces represent median values, dark gray regions show 25 – 75th percentile range, and light gray

regions show 5 – 95th percentile range. Hatched area below 1.0 μm indicates particle size range where fluorescent particles were not considered FBAP due to interference with non-biological aerosol. **(a–b)** Period #7: 7 September 05:46 – 07:26, **(c–d)** Period #8: 26 October 05:54 – 10:34.

Figure S19: Characteristic FBAP number size distribution patterns observed during exemplary periods #9 and #10 (plots analogous to Fig. S16). **(a–b)** Period #9: 15 August 00:08 – 04:48, **(c–d)** Period #10: 19 August 22:59 – 20 August 06:39.

Figure S20: Characteristic FBAP number size distribution patterns observed during exemplary periods #11 and #12 (plots analogous to Fig. S16). **(a–b)** Period #11: 30 September 12:24 – 19:34, **(c–d)** Period #12: 10 September 04:57 – 11 September 03:32.

Figure S21: Average TAP number size distributions for each month of the measurement period. Red traces represent mean values, green traces represent median values, dark gray regions show 25 – 75th percentile range, and light gray regions show 5 – 95th percentile range. Hatched area below 1.0 μm indicates particle size range where fluorescent particles were not considered FBAP due to interference with non-biological aerosol. **(a)** August, **(b)** September, **(c)** October, **(d)** November.

Figure S22: Campaign average TAP number size distribution. Reproduced from Figure 12a, replacing y-axis with logarithmic scale.

Figure S23: Average TAP mass size distributions for each month of the measurement period (plots analogous to Fig. S19). **(a)** August, **(b)** September, **(c)** October, **(d)** November.

Figure S24: Average FBAP mass size distributions for each month of the measurement period (plots analogous to Fig. S19). **(a)** August, **(b)** September, **(c)** October, **(d)** November.

Figure S25: Average size distribution of the FBAP to TAP number concentration ratio ($dN_{F,c} / dN_{T,c}$) for the entire measurement period (plot analogous to Fig. S19). **(a)** August, **(b)** September, **(c)** October, **(d)** November.

Figure S26: Average size distribution of the FBAP to TAP number concentration ratio ($dN_{F,c} / dN_{T,c}$) for the entire measurement period after removing period from 10 – 29 October (plot analogous to Fig. S19).

Channel #	$D_{a,g}$ (μm)	$D_{a,low}$ (μm)	LDC dM ($\mu\text{g m}^{-3}$)	LDC $dM/d\log D_a$ ($\mu\text{g m}^{-3}$)	Campaign Mean Values			
					$dN_{T,c}$ (cm^{-3})	$dN_{F,c}$ (cm^{-3})	$dM_{T,c}$ ($\mu\text{g m}^{-3}$)	$dM_{F,c}$ ($\mu\text{g m}^{-3}$)
1	0.300	-	0.000003	0.000011	0.420	0.00038	0.0059	0.00001
2	0.542	0.523	0.000017	0.000534	0.329	0.00030	0.0274	0.00003
3	0.583	0.562	0.000021	0.000664	0.499	0.00046	0.0518	0.00005
4	0.626	0.604	0.000026	0.000822	0.644	0.00059	0.0828	0.00008
5	0.673	0.649	0.000032	0.00102	0.844	0.00078	0.135	0.00012
6	0.723	0.697	0.000040	0.00127	0.940	0.00089	0.186	0.00018
7	0.777	0.749	0.000049	0.00157	0.949	0.00094	0.233	0.00023
8	0.835	0.805	0.000061	0.00195	0.767	0.00083	0.234	0.00025
9	0.898	0.865	0.000076	0.00243	0.536	0.00067	0.203	0.00025
10	0.965	0.930	0.000094	0.00301	0.367	0.00057	0.173	0.00027
11	1.037	0.999	0.000117	0.00374	0.256	0.00054	0.149	0.00032
12	1.114	1.074	0.000145	0.00463	0.162	0.00048	0.117	0.00035
13	1.197	1.154	0.000180	0.00575	0.120	0.00049	0.108	0.00044
14	1.286	1.240	0.000223	0.00713	0.101	0.00055	0.113	0.00062
15	1.382	1.333	0.000276	0.00885	0.0808	0.00056	0.112	0.00077
16	1.486	1.432	0.000344	0.0110	0.0707	0.00059	0.122	0.00102
17	1.596	1.539	0.000426	0.0136	0.0614	0.00061	0.131	0.00131
18	1.715	1.654	0.000528	0.0169	0.0487	0.00060	0.129	0.00160
19	1.843	1.777	0.000656	0.0210	0.0445	0.00069	0.146	0.00225
20	1.981	1.910	0.000814	0.0261	0.0376	0.00078	0.153	0.00316
21	2.129	2.052	0.00101	0.0323	0.0307	0.00087	0.155	0.00438
22	2.288	2.205	0.00125	0.0401	0.0294	0.00118	0.185	0.0073863
23	2.458	2.370	0.00156	0.0498	0.0238	0.00136	0.185	0.0106
24	2.642	2.547	0.00193	0.0618	0.0214	0.00166	0.206	0.0160
25	2.839	2.737	0.00240	0.0767	0.0182	0.00182	0.218	0.0218
26	3.051	2.941	0.00297	0.0952	0.0159	0.00195	0.237	0.0290
27	3.278	3.160	0.00369	0.118	0.0131	0.00190	0.242	0.0351
28	3.523	3.396	0.00458	0.147	0.0108	0.00180	0.246	0.0413
29	3.786	3.650	0.00568	0.182	0.00866	0.00160	0.246	0.0454
30	4.068	3.922	0.00705	0.226	0.00691	0.00138	0.244	0.0488
31	4.371	4.215	0.00875	0.280	0.00549	0.00117	0.240	0.0510
32	4.698	4.529	0.0109	0.347	0.00430	0.00096	0.234	0.0519
33	5.048	4.867	0.0135	0.431	0.00320	0.00073	0.216	0.0493
34	5.425	5.230	0.0167	0.535	0.00242	0.00057	0.203	0.0479
35	5.829	5.620	0.0207	0.664	0.00187	0.00045	0.193	0.0463
36	6.264	6.040	0.0257	0.824	0.00157	0.00039	0.202	0.0499
37	6.732	6.490	0.0319	1.02	0.00122	0.00032	0.195	0.0517
38	7.234	6.974	0.0396	1.27	0.00102	0.00029	0.202	0.0572
39	7.774	7.495	0.0492	1.57	0.00079	0.00024	0.195	0.0588
40	8.354	8.054	0.0611	1.95	0.00061	0.00019	0.185	0.0585
41	8.977	8.655	0.0758	2.42	0.00045	0.00014	0.169	0.0544
42	9.647	9.300	0.0940	3.01	0.00033	0.00011	0.157	0.0499
43	10.370	9.994	0.117	3.74	0.00024	0.00008	0.141	0.0449
44	11.140	10.740	0.145	4.63	0.00018	0.00005	0.128	0.0391
45	11.970	11.541	0.180	5.75	0.00014	0.00004	0.124	0.0381
46	12.860	12.402	0.223	7.13	0.00013	0.00006	0.145	0.0619
47	13.820	13.328	0.276	8.85	0.00011	0.00004	0.146	0.0577
48	14.860	14.322	0.344	11.00	0.00010	0.00003	0.166	0.0595
49	15.960	15.390	0.426	13.62	0.00008	0.00002	0.168	0.0354
50	17.150	16.539	0.528	16.90	0.00007	0.00001	0.182	0.01546
51	18.430	17.773	0.656	20.98	0.00007	0.000002	0.214	0.00759
52	19.810	19.099	0.814	26.05	0.00006	0.000001	0.258	0.00526

Table S1.

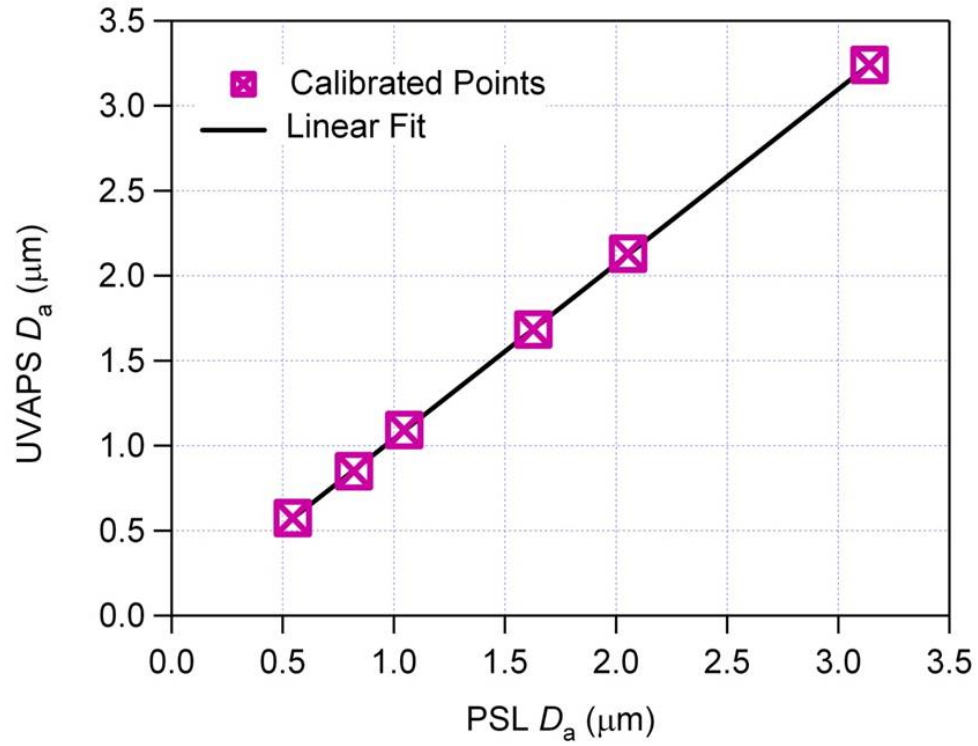


Figure S1.

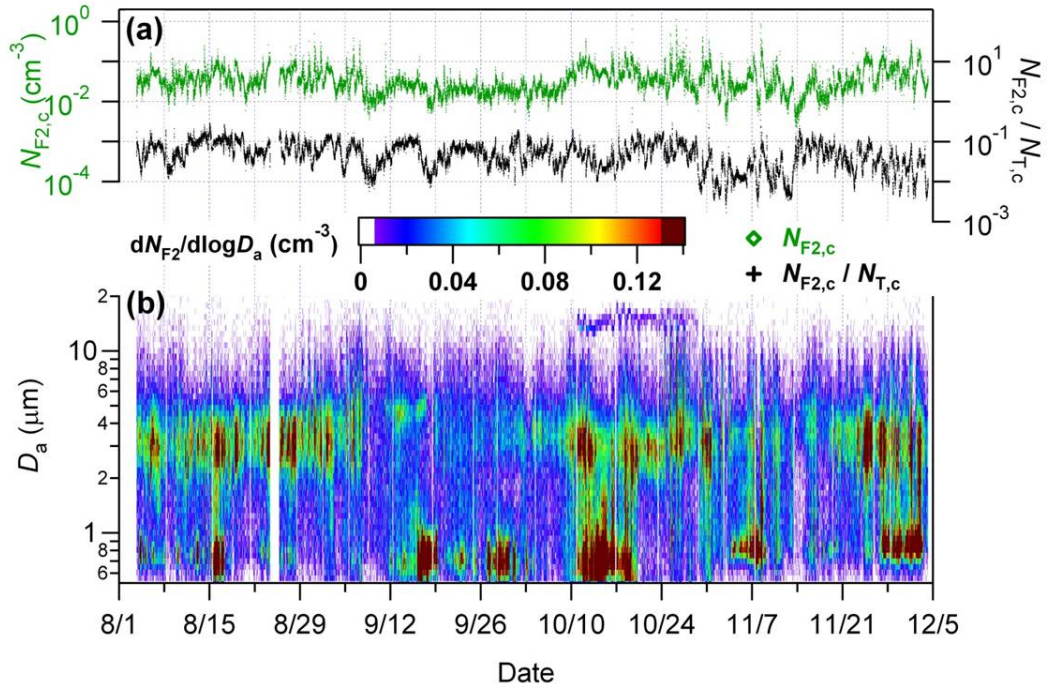


Figure S2.

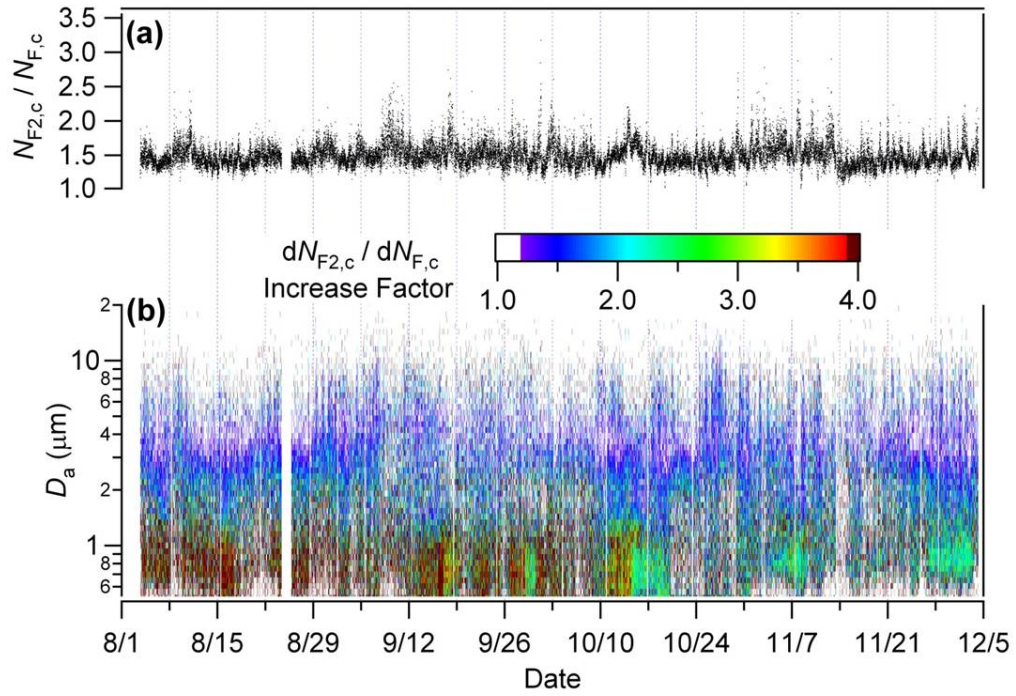


Figure S3.

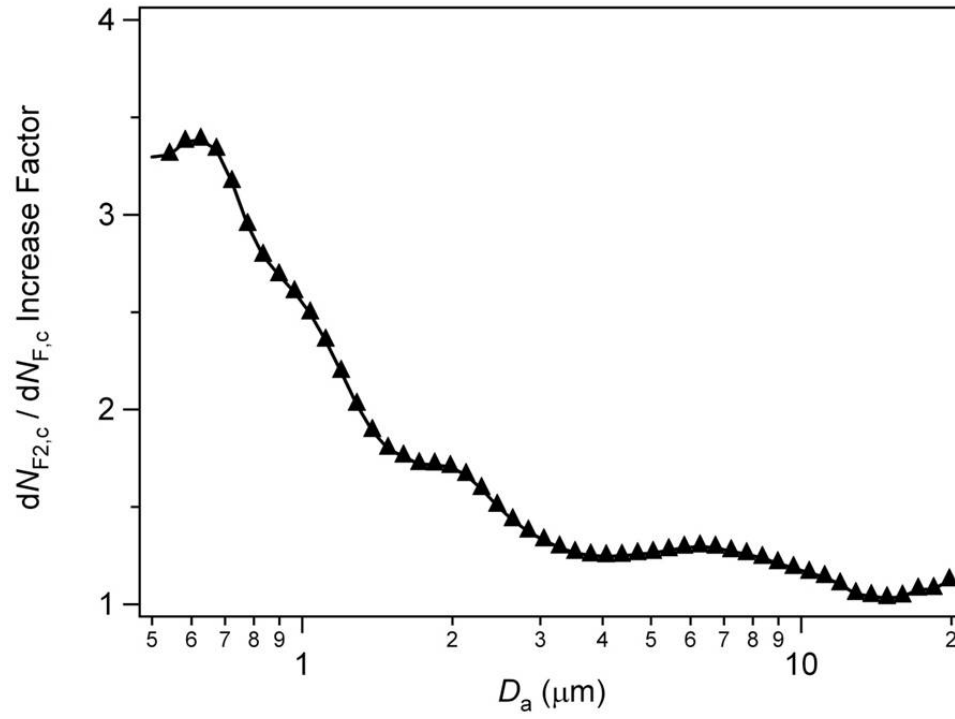


Figure S4.

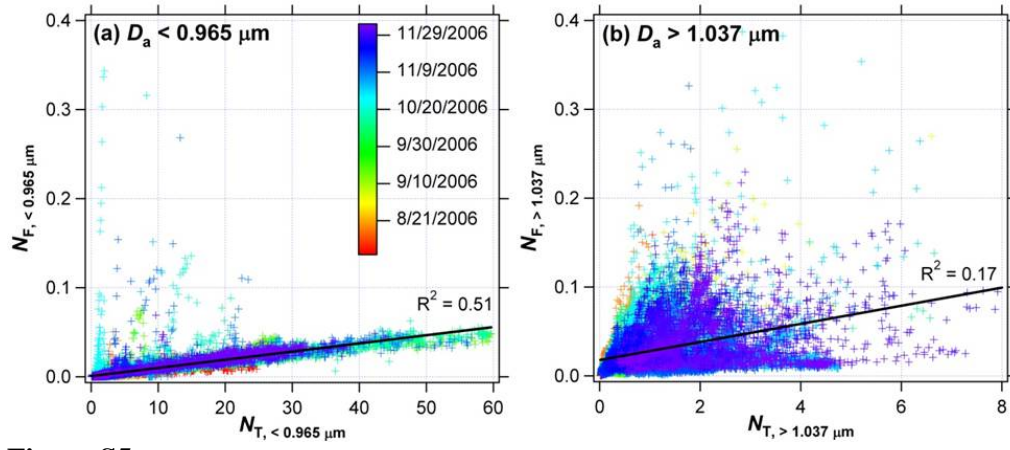


Figure S5.

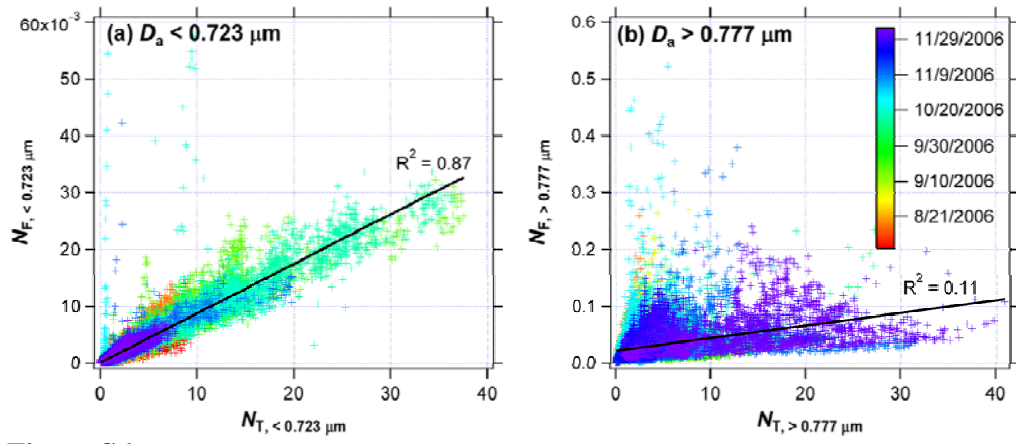


Figure S6.

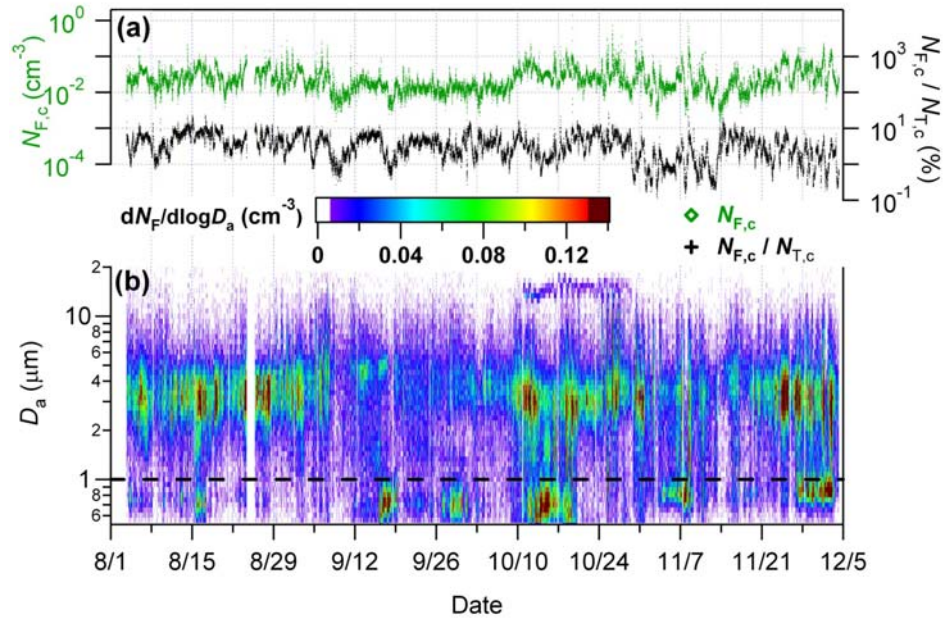


Figure S7.

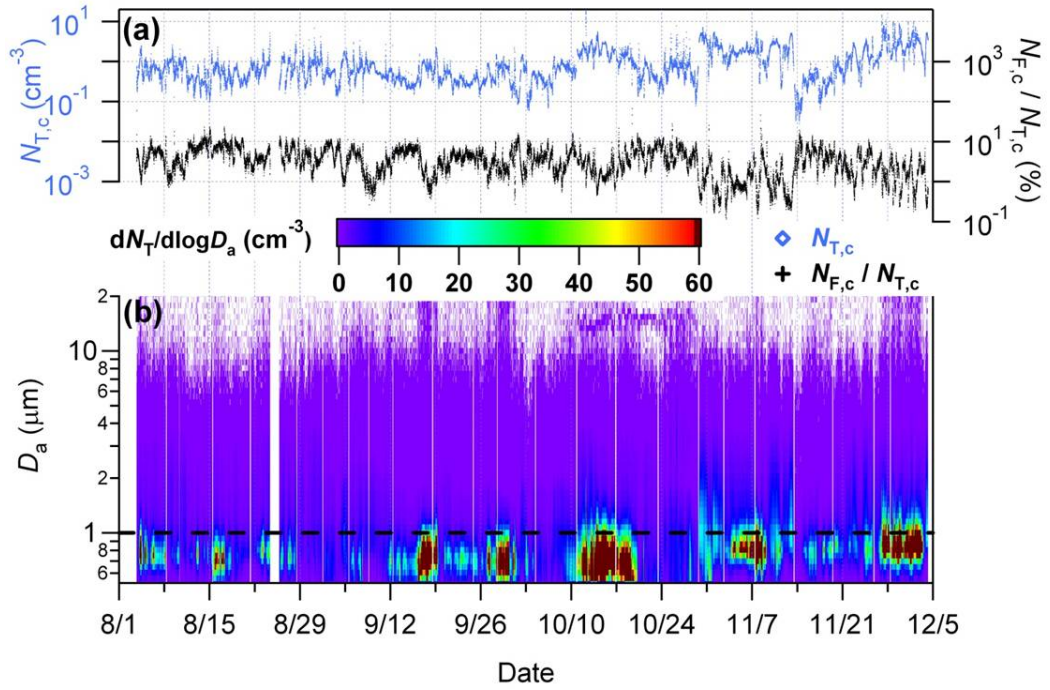


Figure S8.

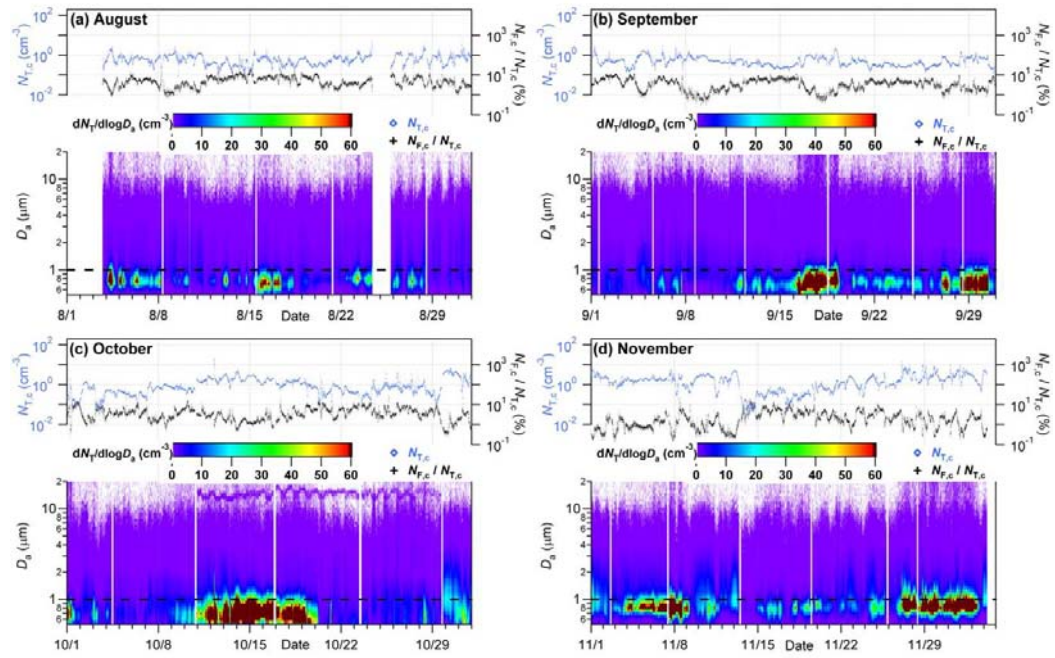


Figure S9.

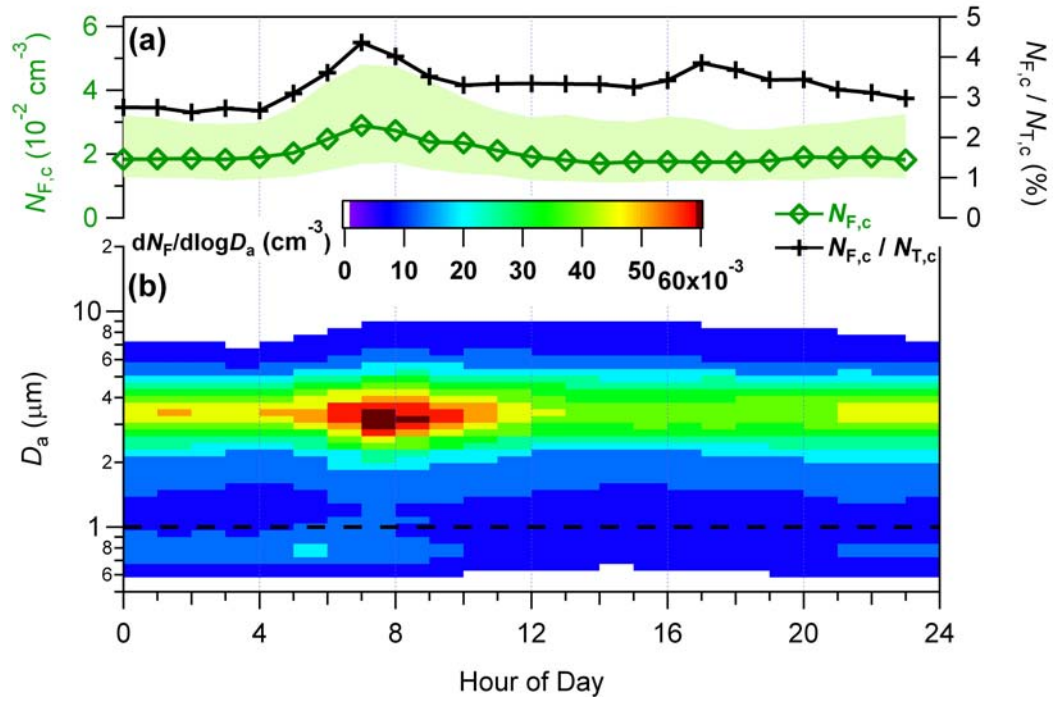


Figure S10.

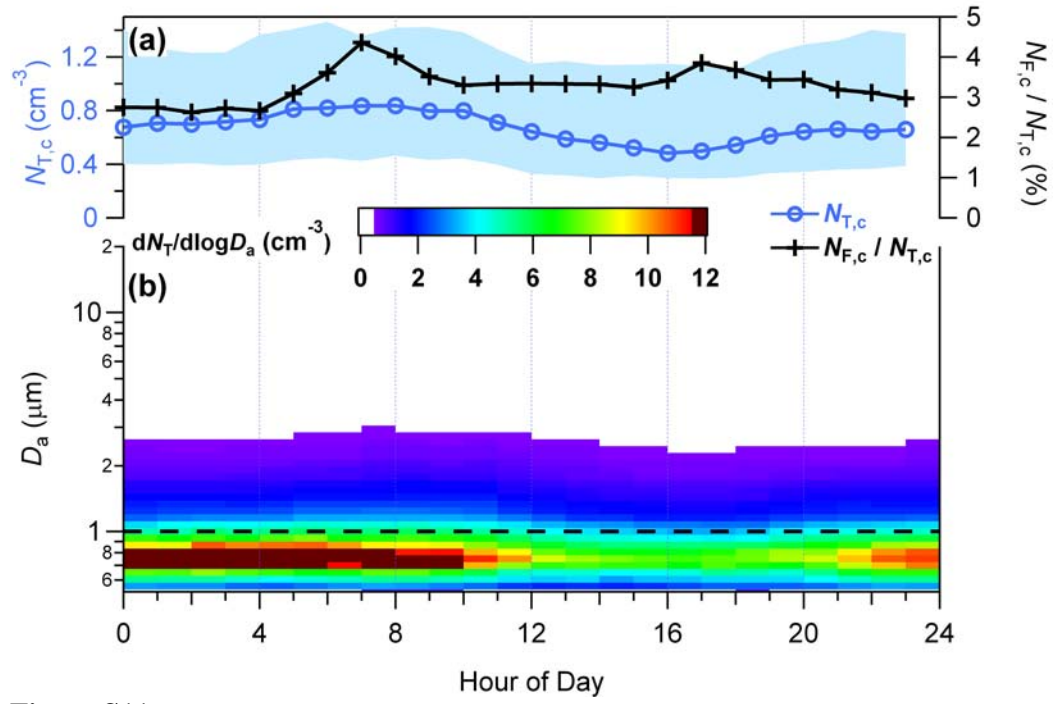


Figure S11.

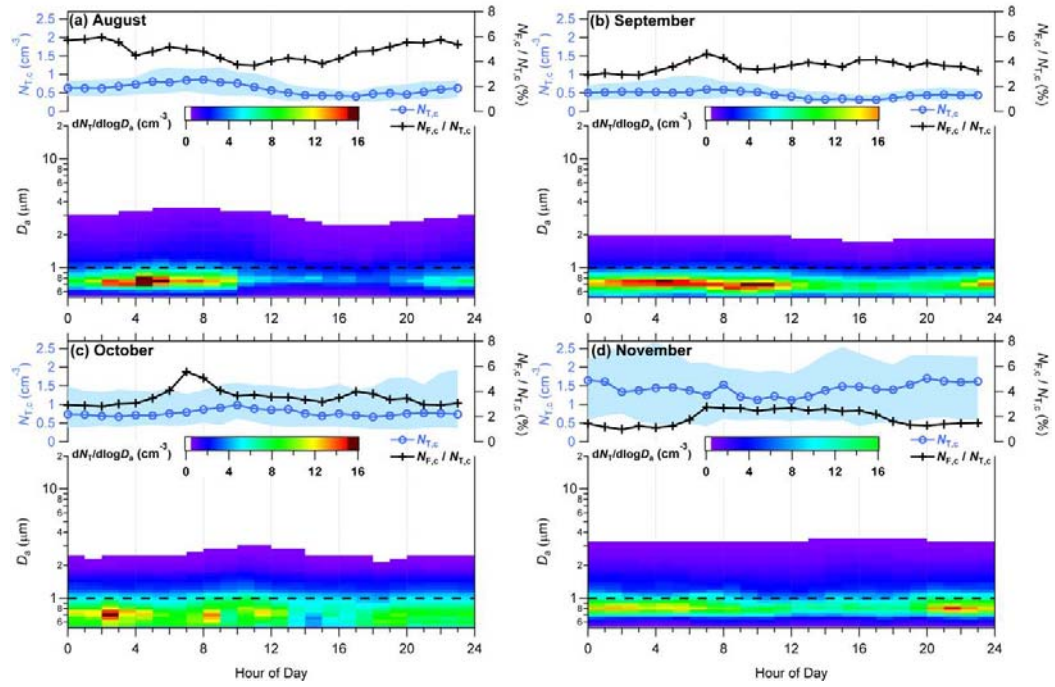


Figure S12.

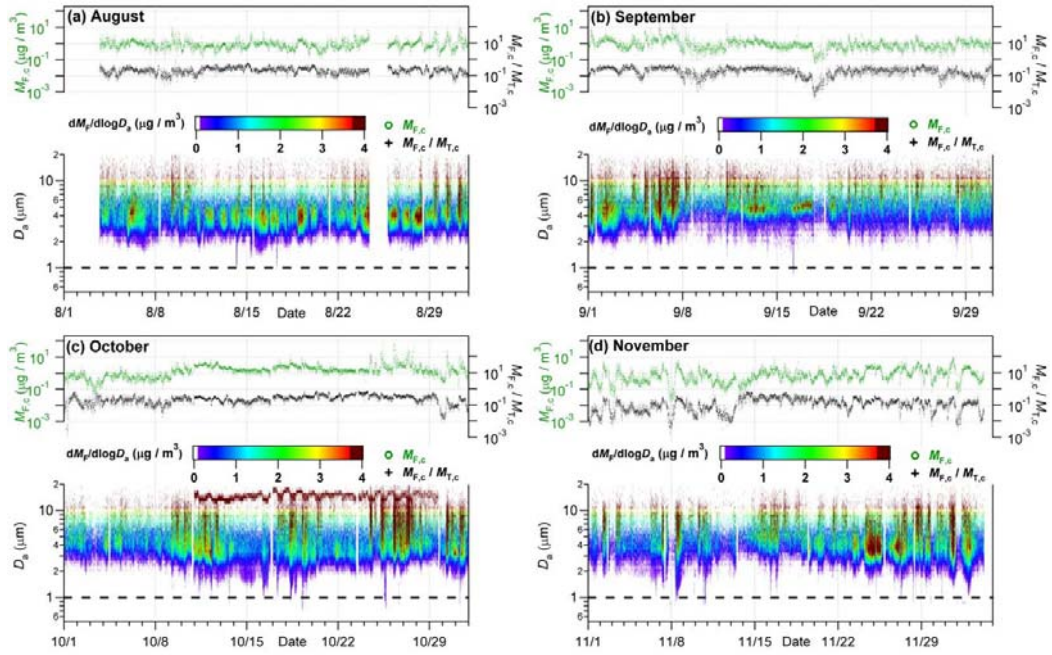


Figure S13.

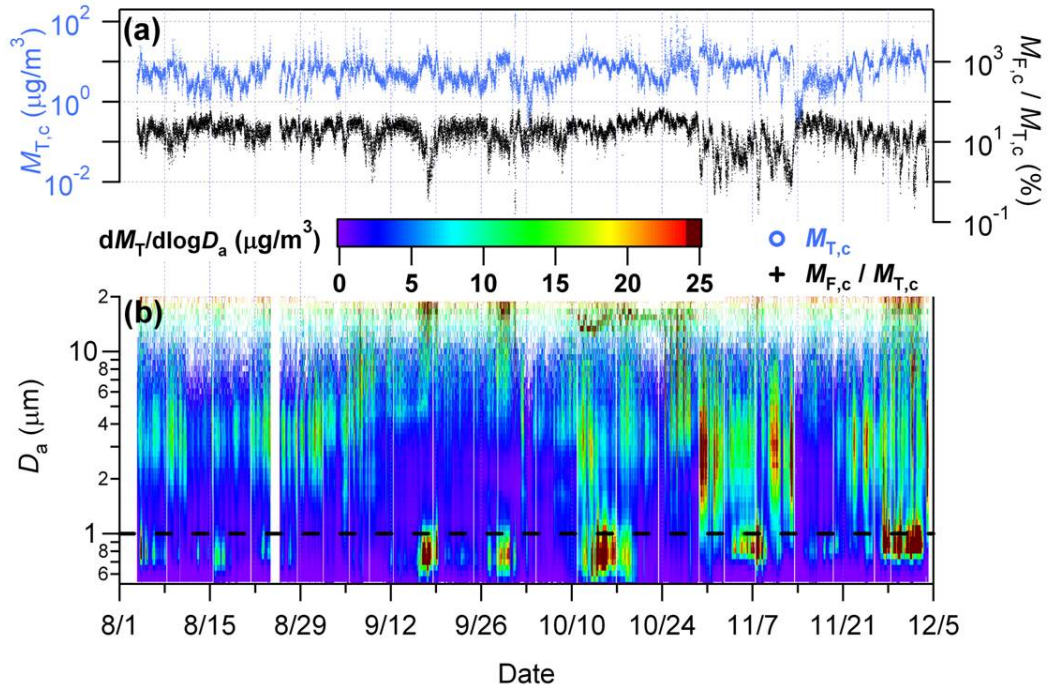


Figure S14.

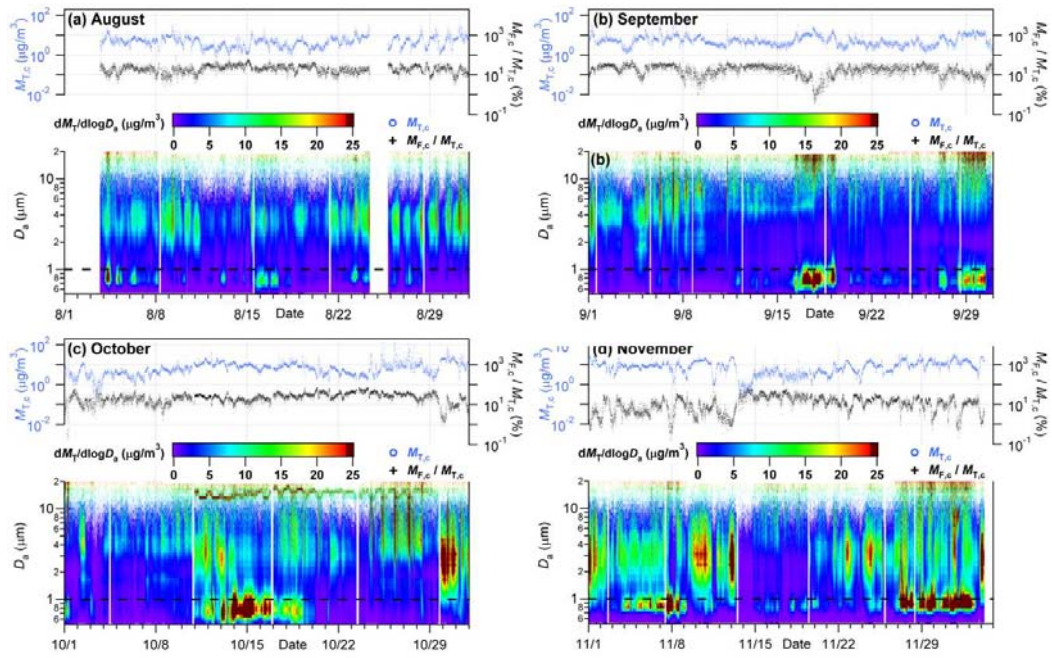


Figure S15.

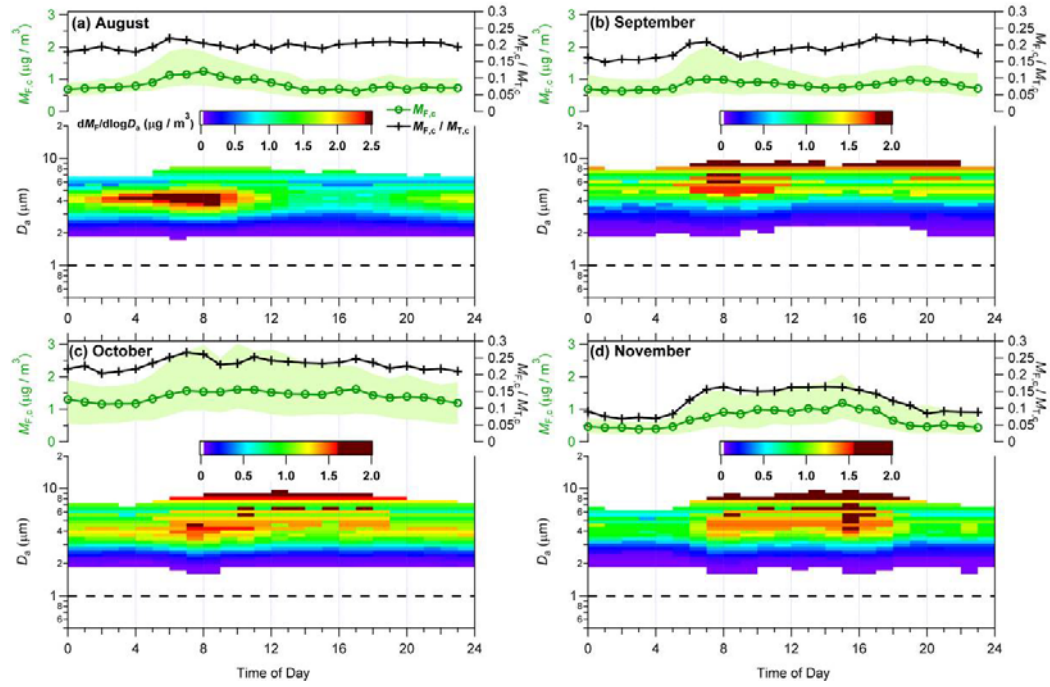


Figure S16.

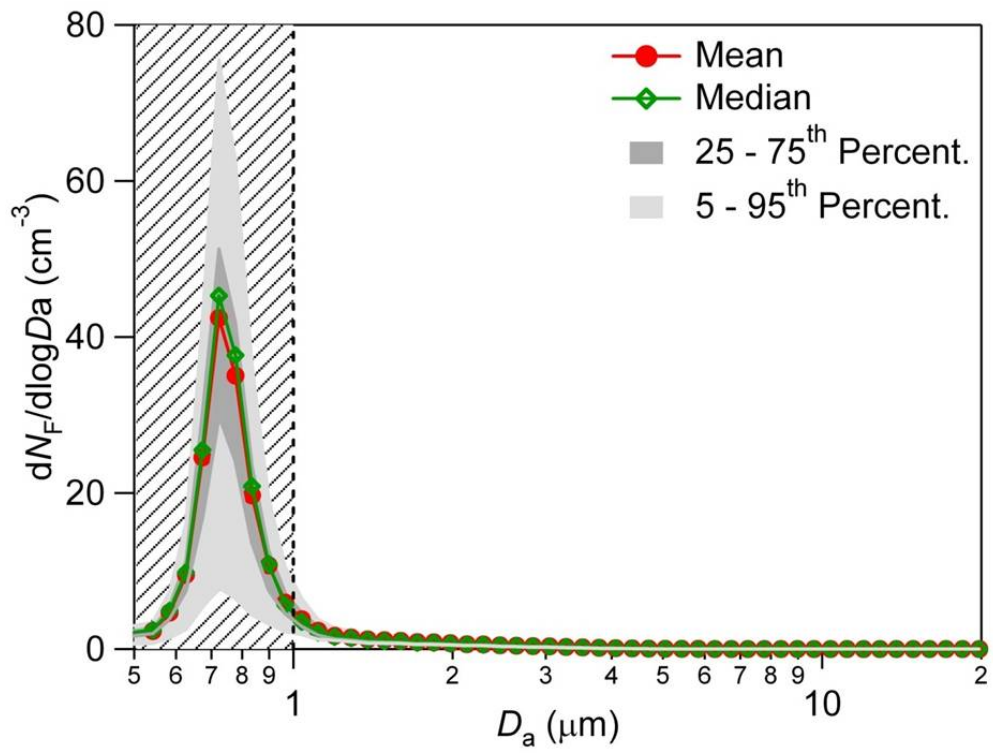


Figure S17.

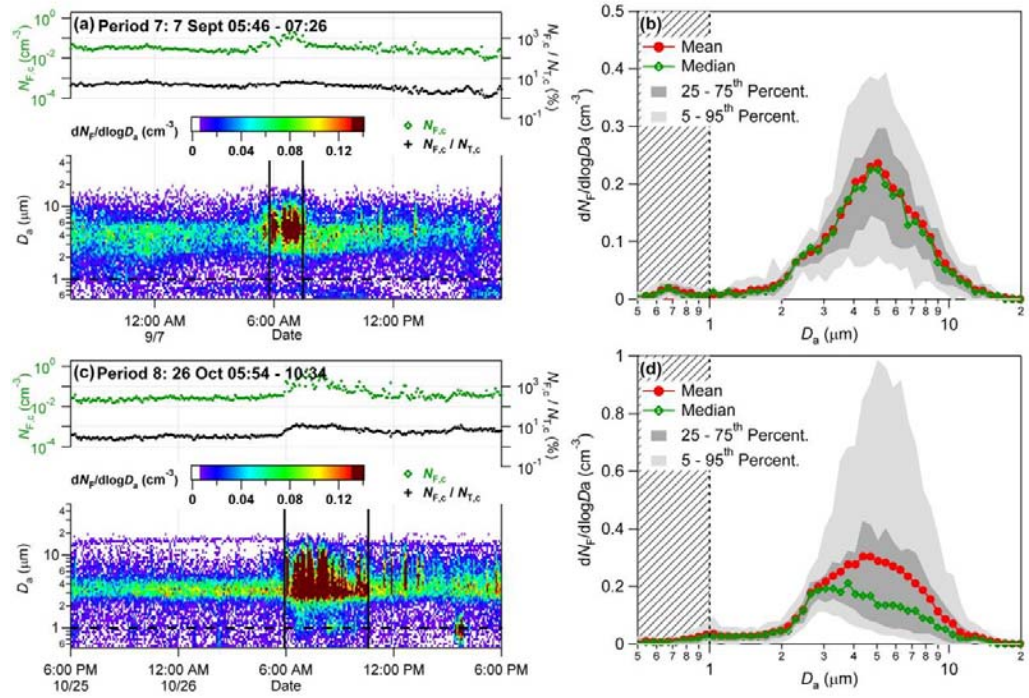


Figure S18.

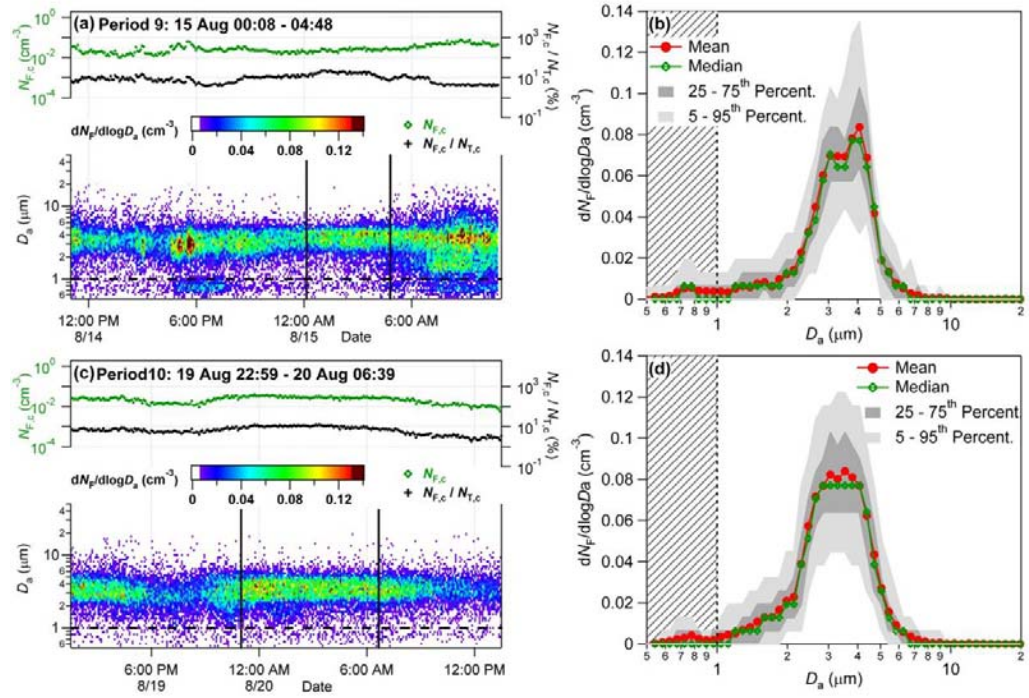


Figure S19.

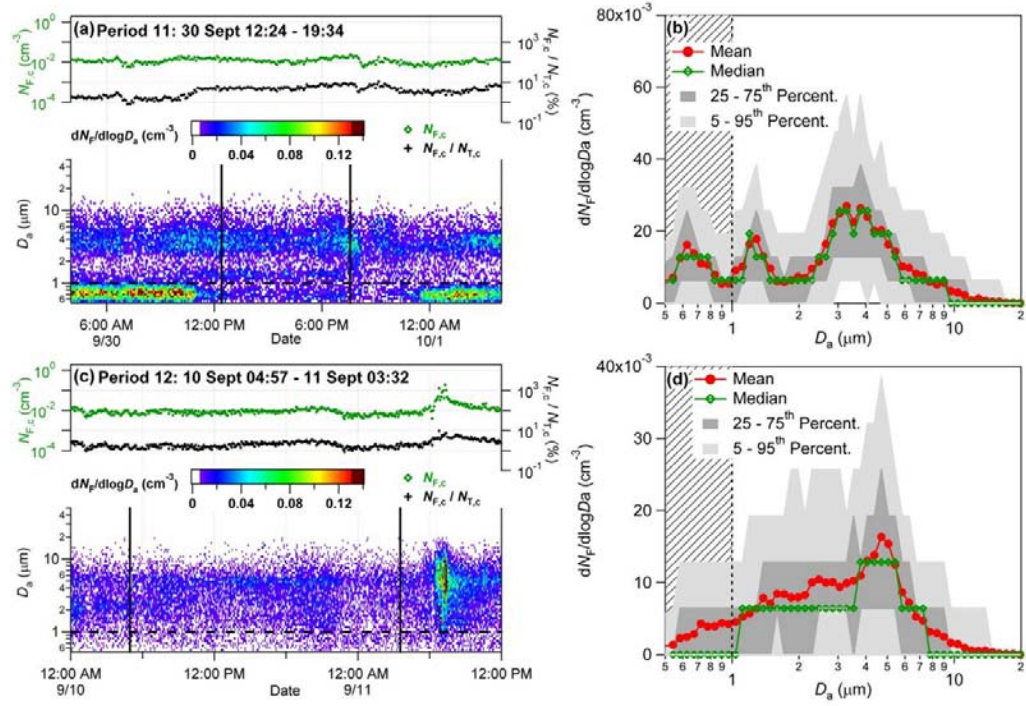


Figure S20.

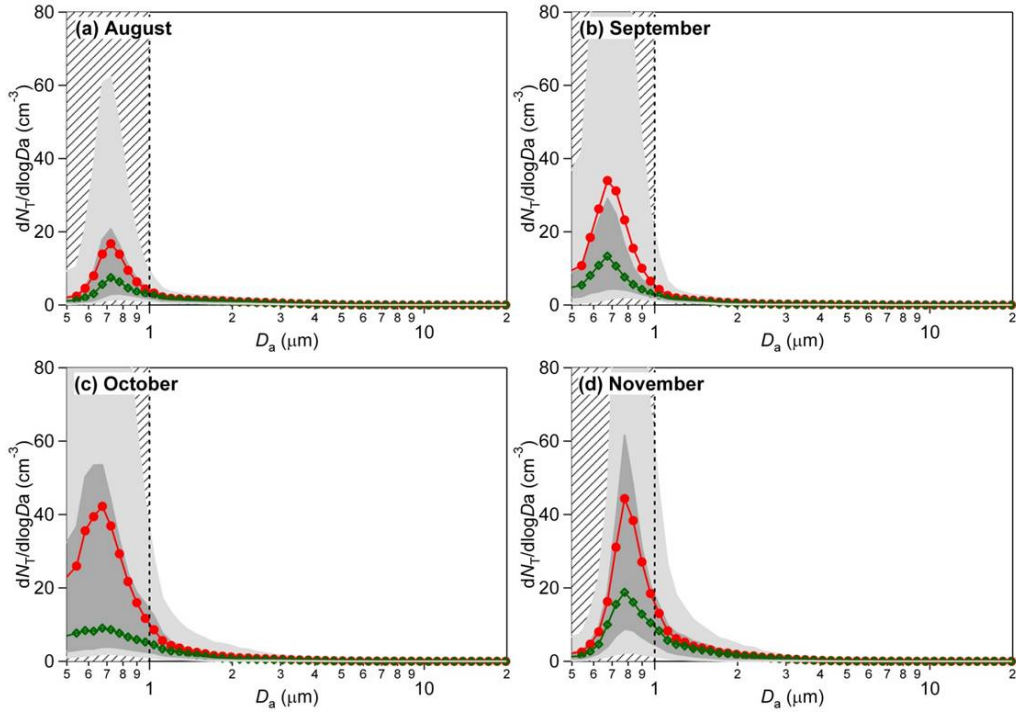


Figure S21.

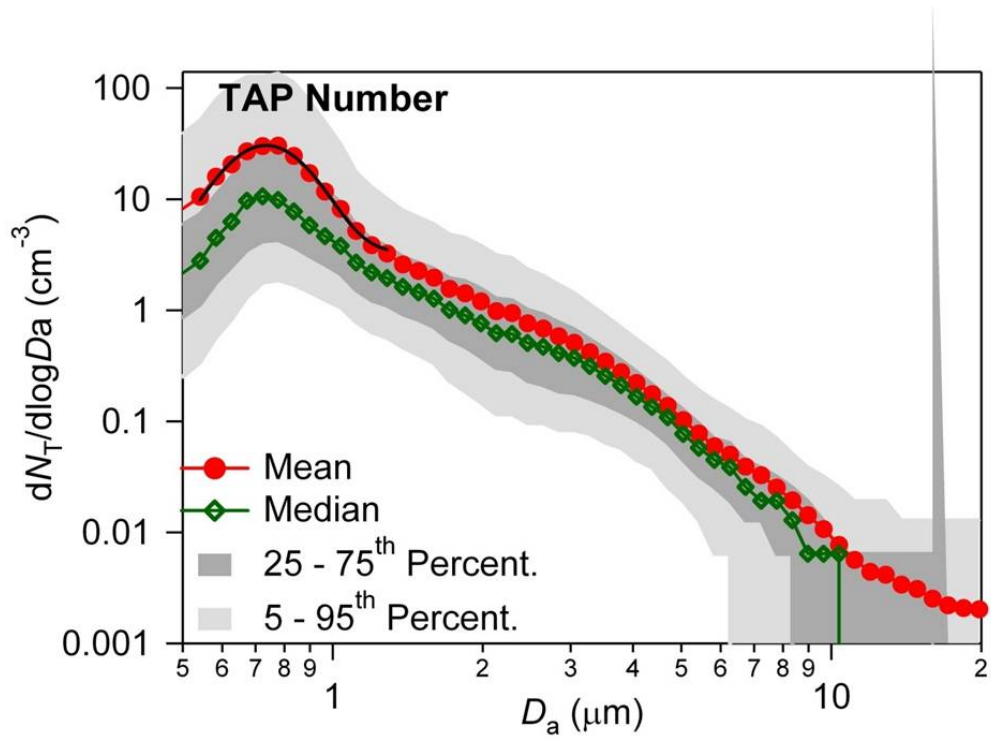


Figure S22.

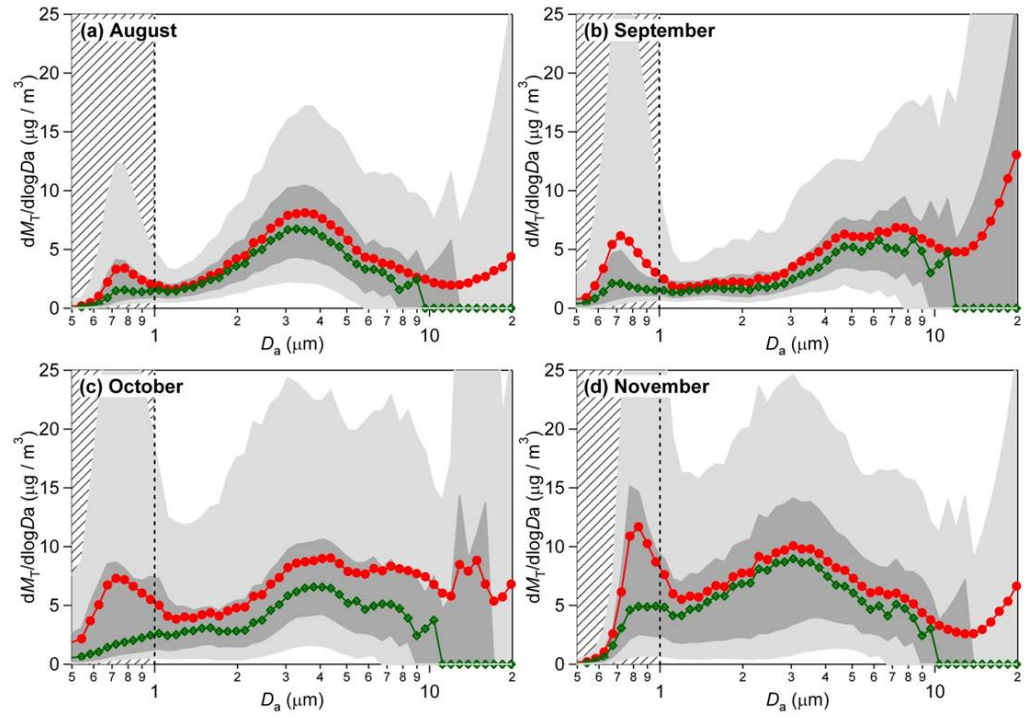
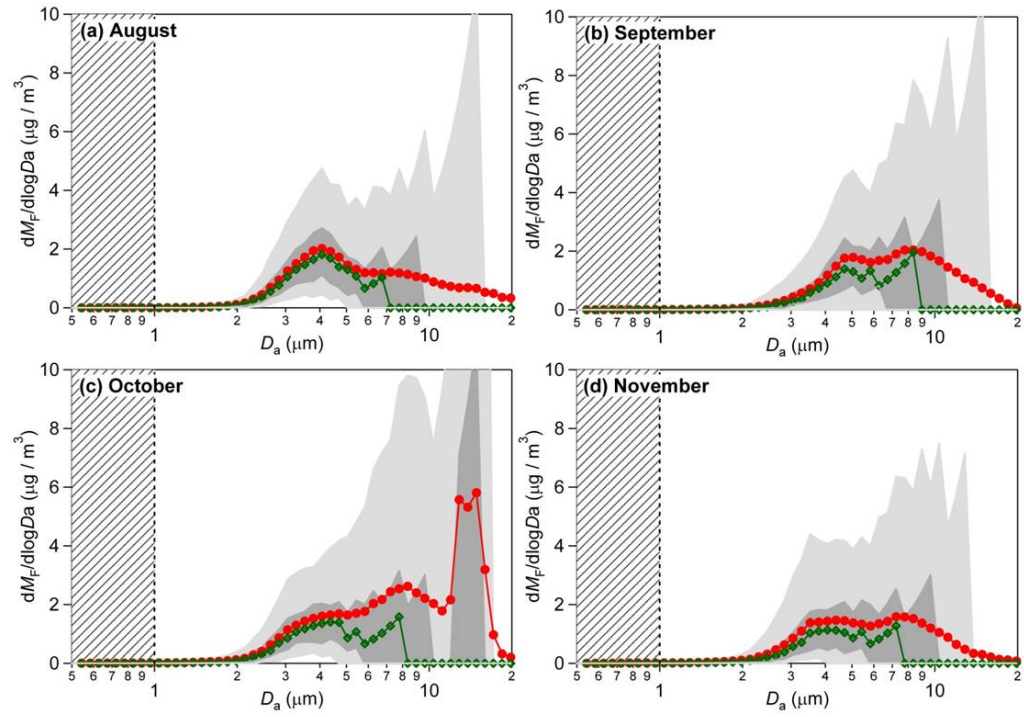
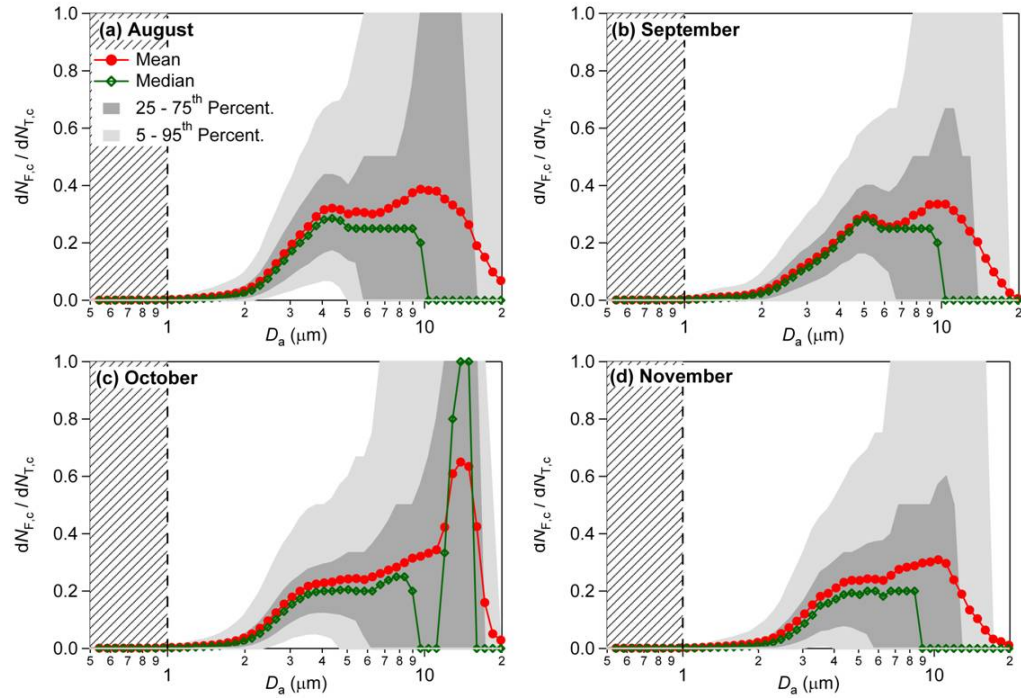


Figure S23.

**Figure S24.**

**Figure S25.**

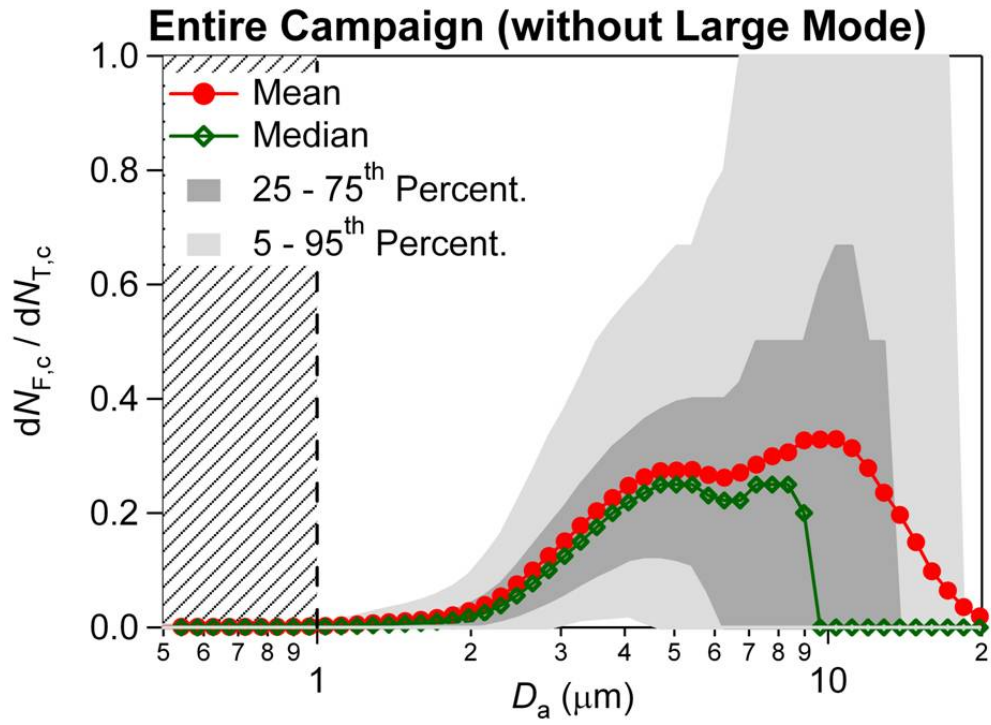


Figure S26.